Cement and Concrete Composites 118 (2021) 103931

Contents lists available at ScienceDirect

Cement and Concrete Composites

journal homepage: http://www.elsevier.com/locate/cemconcomp

Evolution of elastic and thermal properties of cementitious composites containing micro-size lightweight fillers after exposure to elevated temperature

Zhenglai Shen [a], Hongyu Zhou [a,*], Adam Brooks [a], Dominic Hanna [b]

[a] Department of Civil and Environmental Engineering, University of Tennessee, Knoxville, TN, 37996, USA
[b] Moffatt & Nichol Inc., Raleigh, NC, 27609, USA

ARTICLE INFO

Keywords:
Cementitious composites
Thermal damage
Lightweight fillers
Micro-mechanics model

ABSTRACT

This paper studies the evolution of elastic and thermal properties of cementitious composites containing micro-size lightweight fillers after exposure to elevated temperatures (up to 800 °C). A multiscale investigation is carried out to study the thermal degradation of cementitious composite materials at multiple scale levels: at cement past level, the dehydration kinetics of cement hydrates (i.e., C–S–H, CH and aluminate hydrates) and development of microcracks are studied as functions of exposure temperatures. The damage mechanism of the inclusion phases and damages within the interfacial transition zone (ITZ) under elevated temperature are also investigated. In addition, the change of mechanical (i.e., elastic moduli, compressive strengths) and thermal (thermal conductivities) properties are measured as functions of the exposure temperature. Based on the experimental studies, a multiscale thermal degradation model is developed where the thermal degradations of cement paste (including water composition, porosity, and solid phase changes), inclusion phases, and the interfaces are captured through a multiscale sub-stepping homogenization scheme. The thermal degradation model is validated through multiple sets of experimental data. Finally, the influence of key parameters including the particle size distribution of the inclusions, the chemical composition, as well as the effects of ITZ damage are studied.

1. Introduction

Functional cementitious composite materials containing micro- and meso-size particulate or fibrous inclusions have been increasing studied in the past decade [1–4]. Some examples of this class of materials include lightweight and ultra-lightweight cementitious composites (LWCC/ULCC) made from hollow fly-ash cenosphere (FAC) and hollow glass microspheres (HGM) [1–3,5,6], oil-well cement containing glass microspheres [7], phase change material (PCM) cement composites which contains microencapsulated PCM particles for thermal energy storage, and self-healing cementitious composites which incorporate core-shell microcapsules filled with healing agents such as mineral compounds and bacteria [8,9]. In particular, LWCC/ULCC has been studied for various structural purposes due to its promising mechanical and physical properties, including the use in wall constructions for energy-efficient buildings [10,11] and as structural fill in steel-concrete-steel sandwich composite structures for offshore and building structures [12,13].

As one of the major hazards to building structures, fire jeopardizes structural integrity and life safety of the residents. While concrete is considered as a good fire resistance material, it is also well-recognized that elevated temperature (>300 °C) causes chemical composition change in cement-based materials, and consequently, substantial reductions in strength and elastic modulus [14]. In particular, with the increased application of LWCC/ULCC, the risk of fire exposure increases as well. Cementitious materials undergo complex multiphase thermal, hydraulic, mechanical and chemical processes when subjected to high temperatures – i.e., the hydration products in cement paste such as calcium-silicate-hydrate (C–S–H) and calcium hydroxide (CH) dehydrate or decompose at elevated temperatures, which can lead to micro-cracking and pore-coarsening [15]. Thermal deterioration also occurs for certain type of aggregates (e.g., limestone) under the temperature range of building fire [16]. The pressure built-up in its micro-pore systems can lead to cracking and explosive spalling [17]. In

* Corresponding author. 851 Neyland Drive, 417 John D. Tickle Building, Knoxville, TN, 37996-2313, USA.
E-mail address: hzhou8@utk.edu (H. Zhou).

https://doi.org/10.1016/j.cemconcomp.2021.103931
Received 8 June 2020; Received in revised form 9 December 2020; Accepted 5 January 2021
Available online 11 January 2021

addition, the fire behavior of cementitious composites strongly depends on the type of inclusions (e.g., fiber, micro-sized particles) [18], it is important to understand the deterioration mechanisms and interactions among material phases during and after fire exposures. To date, most existing researches focused on high temperature performance of normal weight concrete [19–21], high strength concrete [22–24], and lightweight aggregate concrete [25–28]. Recently, LWCC/ULCC containing fly-ash cenospheres has been investigated as a thermal insulating material for buildings [29] because of its good high temperature performance. Huang et al. [30,31] studied the mechanical behavior (i.e., compressive strength, flexural strength, elastic modulus) and micro-structure changes of ULCC containing FAC and synthetic micro-fibers/steel fibers under temperatures up to 900 °C. These studies provided valuable experimental evidences on the mechanical property change and micro-structural evolution of LWCC/ULCC after exposure to elevated temperatures. However, the underlying mechanisms of its property deterioration and its relations to microstructural change has not been well understood. Moreover, the empirical expressions based on specific sets of experimental data can hardly be extended to other materials with, for example, different volumes and types of functional additives. Therefore, a quantitative understanding on the evolution of elastic and thermal properties of LWCC/ULCC after exposure to elevated temperature is needed to establish this important relationship.

Although a number of studies to date have been carried out to study the behavior of concrete and cement paste after exposure to high temperature, few analytical models have been developed for functional cementitious composites containing micro-size particular inclusions or fibers [32]. Zhao et al. [33] analyzed the thermal decomposition of hardened cement paste based on the kinetic and stoichiometric analysis. Using the thermal decomposition prediction, the authors [34] further modeled the elastic modulus of hardened cement paste after exposure to elevated temperatures by using a simple micromechanics based composite model. More recently, Jiang et al. [35] analytically studied the instantaneous phase compositions of cement pastes under elevated temperatures (up to 1200 °C). The result shows that the phase compositions of cement paste are sensitive to the heating rates and highlighted the need of considering temperature history in analyzing concrete structures exposure to fires. Moreover, a multiscale model was developed by Zhang et al. [32] to predict the thermal damage of hybrid fiber-reinforced concrete. The multiscale model includes four scale levels, i.e., the C–S–H product level, the cement paste level, the concrete level, and the hybrid fiber-reinforced concrete level. While it is generally applicable, the model is very complex and involves many sub-steps and parameters which may make it difficult to implement. Therefore, a model is desired to predict the properties of cementitious composites with particular or fibrous inclusions after exposure to elevated temperatures, especially at composite level where thermal degradation phenomena at multiple length scale is considered.

In this paper, a comprehensive study is carried out to investigate how the physicochemical, microstructural, and mechanical properties of cementitious composites containing micro-size fillers evolve under elevated temperatures. First, experimental investigations were carried out to gain insights into the damage mechanisms of lightweight cementitious composites containing FACs – from the thermal degradation of cement paste, micro-cracking, to the thermal damage evolution in the interfacial transition zone (ITZ). Simultaneous thermogravimetry and differential scanning calorimetry (TGA-DSC), X-ray diffraction (XRD), and X-ray fluorescence (XRF) tests were performed to quantify the decomposition of cementitious composites and fly-ash cenospheres (FACs) after exposure to elevated temperatures. Mechanical and thermal tests were conducted to elucidate the changes of the mechanical properties (elastic modulus and compressive strength) and the thermal conductivity as functions of temperature. Then, a multiscale thermal degradation model is developed to predict the elastic modulus evolution of cementitious composites containing FACs after exposure to high temperature. The model considers several degradation mechanisms including the thermal decomposition and microcracks developed in cement paste, as well as the interfacial thermal damage between cement paste and inclusion phases.

2. Experimental program

2.1. Material preparation and thermal loading

To investigate the damage mechanism of cementitious composites after exposure to elevated temperatures, lightweight cement composites (LWCC) specimens with different types and volume fractions of fly-ash cenosphere (FAC) were made. ASTM C150 compliant Type I/II ordinary Portland cement (OPC), Ottawa silica sand, grounded quartz/silica flour, and two different types of fly-ash cenospheres (FAC) with different particle size distributions – i.e., CenoStar ES106 (particle size $D < 106$ μm) and ES200/600 (200 μm $< D <$ 600 μm) were used to prepare the mortar materials for experiments. The particle size distributions of FACs (ES106 and ES200/600), quartz flour, and silica sand are plotted in Fig. 1 (a). The FACs were added at volume fractions of 7%, 14%, 21%, 28% to replace the fine aggregates (silica sand and quartz flour) through volume equivalency. Detailed mix proportions are listed in Table 1. Water cement ratio (w/c) of 0.33 was used for all specimens, and a polycarboxilic ether-based superplasticizer was used to adjust the workability of the mixtures.

For each specimen group, 25 cylinder specimens with a 50 mm in diameter and 100 mm in height were prepared in one batch to investigate the effects of the type and volume fraction of FAC on mechanical properties and microstructure of LWCC after exposure to temperatures up to 800 °C. Specimens were demolded after two days and cured in a temperature-controlled water bath (25 °C) until 28 days. The specimens were then placed in a convection oven for 48 h at 105 °C to remove capillary water before being heated to the prescribed temperatures using a programmable muffle furnace.

Except for the control specimen group which was kept under room temperature around 25 °C, all other specimens were heated to their designated exposure temperatures (i.e., 200 °C, 400 °C, 600 °C, and 800 °C) following the heating profiles as shown in Fig. 1 (b). Specimens were heated at a constant rate of 0.5 °C/min to minimize thermal shock and temperature stresses. The specimens were maintained at the target temperatures for 3 h to ensure uniform temperature distribution across the entire specimen, before they were cooled to room temperature at a constant rate of 0.5 °C/min. Immediately after they were removed from the furnace, the specimens were weighted to determine the weight loss and sealed in plastic bags to prevent water absorption. Color changes were observed for samples heated at each target temperature – i.e., specimens that were heated between 200 °C and 600 °C exhibited a yellowish color that progressively darkened as the heating temperature increases, see Fig. 1 (b); specimens heated to 800 °C exhibited a pinkish red color that is mainly attributed to the formation of silicate and mullite in the temperature range between 600 °C and 800 °C [30]. Minimal surface cracking was observed on specimens exposed to 200 °C and 400 °C. At 600 °C, web-like hairline cracks were observed on the specimen surface. For specimens heated to 800 °C, cracking was notably more severe across the sample volume. Since both heating and cooling were controlled at a low rate (0.5 °C/min), the specimen cracking is most likely due to the volume shrinkage caused by dehydration and that chemical change took place as a result of heating, as well as the non-uniform thermal expansion/shrinkage of the mortar constituents. All heated specimens maintained integrity and no spalling was observed.

2.2. Thermal degradation and microstructural evaluation

Fig. 2 (a) and Table 2 present the simultaneous thermogravimetry and differential scanning calorimetry (TGA-DSC) and XRF results. The primary contents of fly-ash cenospheres (FACs) are silicates (represented by SiO_2 in XRF) and aluminates (represented by Al_2O_3 in XRF results),

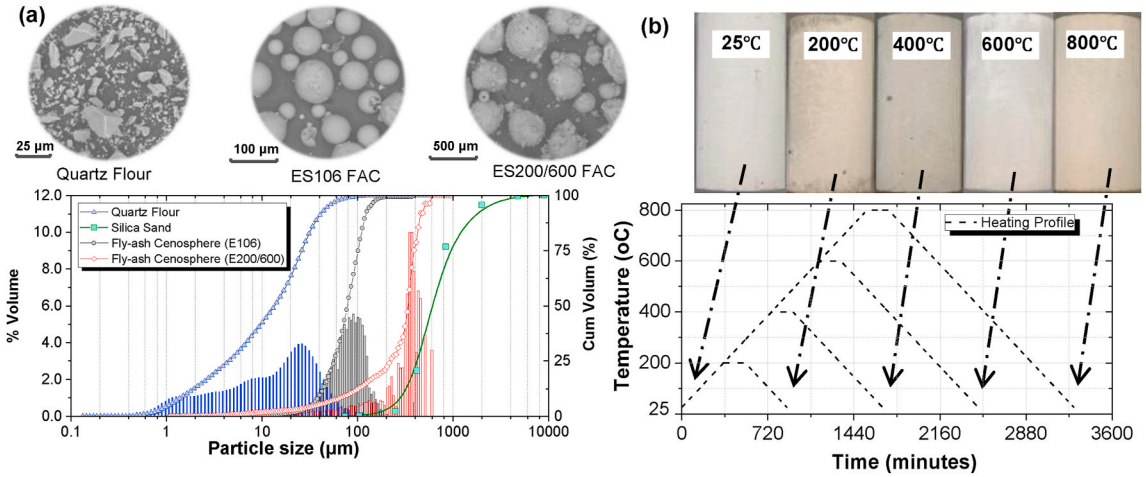

Fig. 1. (a) Particle size distributions, (b) heating profiles and pictures showing the surface color change after exposed to various temperatures. (For interpretation of the references to color in this figure legend, the reader is referred to the Web version of this article.)

Table 1
Test matrix and mix proportions (by weight, kg of materials/m^3 of concrete).

Mix ID	Cement	Water	W/C	FAC[a]	Silica Sand[b]	Quartz Powder[b]	FAC vol%
Control	692.4	225	0.33	0	1163.21	70.06	0
ES106-07	692.4	225		63.66	1016.65	61.23	7%
ES106-14				136.40	849.14	51.14	14%
ES106-21				200.57	701.42	42.24	21%
ES106-28				272.81	535.08	32.23	28%
ES200/600-07	692.4	225		57.36	1016.65	61.23	7%
ES200/600 -14				122.91	849.14	51.14	14%
ES200/600 -21				180.73	701.42	42.24	21%
ES200/600 -28				245.83	535.08	32.23	28%

[a] The true density of fly-ash cenosphere (FAC) are 910 kg/m^3 and 820 kg/m^3 for ES106 and ES200/600, respectively.
[b] The density of silica sand and quartz powder are 2650 kg/m^3.

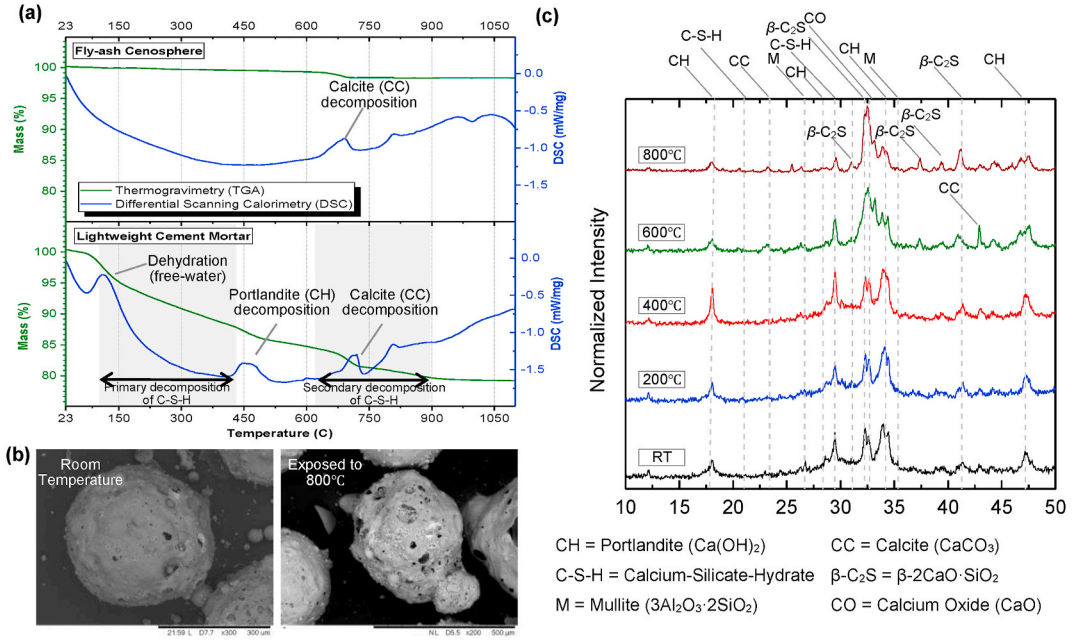

Fig. 2. (a) Simultaneous thermogravimetry and differential scanning calorimetry (TGA-DSC) results for fly-ash cenosphere and LWC mortar (7% FAC) heated up to 1200 °C; (b) SEM image showing FAC before and after exposure to elevated temperatures; and (c) X-ray diffraction (XRD) results for LWC mortar (without silica sand) exposed to high temperatures.

Table 2
X-ray fluorescence (XRF) results of fly-ash cenosphere (FAC) before and after exposure to 800 °C.

Chemical composition		Na_2O (%)	MgO	Al_2O_3	SiO_2	P_2O_5	SO_3	K_2O	CaO	TiO_2	Fe_2O_3
FAC	Room Temp	0	1.5	37.8	52.1	0.5	0.3	2	2.6	1.1	1.9
	800 °C	0	1.7	37.6	51.8	0.5	0.3	2.1	2.7	1.2	1.9

which exceed 80% of the mass. After exposure to elevated temperature (800 °C), there is no noticeable compound change taking place, although small amount (less than 5%) of mass loss was observed up to 675 °C. This may be caused by the structural reorganization of metasilicates in the presence of calcium oxide [36] and small amounts of $CaCO_3$ decomposes at around 675 °C, which is reflected as the surface morphology changes of FAC before and after exposure to high temperature, as shown in the SEM images in Fig. 2 (b). Similar to FAC, silica sand may also loss a small amount of mass due to the formation of siloxane bridges resulting from dihydroxylation of isolated silanol groups on the internal surface of the sand at temperature around 723 °C [37]. Therefore, the mass loss of LWCC is mostly attributed to the dehydration and thermal deterioration of cement hydration products.

Within the cement paste, gradual mass loss takes place from room temperature up to around 950 °C. This is mainly attributed to the loss of capillary free water, physically absorbed water, and chemically bound water in calcium silicate hydrate (C–S–H) and calcium hydroxide (CH) at different temperatures. The loss of capillary water and physically absorbed water takes place when the concrete is heated up to 400 °C; whereas chemically bound water is a part of cement hydration compounds which could not be released from the cement paste until the chemical decomposition of C–S–H and CH occurring at a high temperatures [30]. A significant mass loss is observed at 105 °C mainly due to the evaporation of free water and the decomposition of ettringite. Gradual mass loss was observed between 105 °C and 450 °C, where the primary dehydration of C–S–H takes place at this temperature range via loss of physically bound water, such as absorbed water in its gel pores and interlayer water which is more tightly bound within its interlayer spaces [38]. Drastic mass loss between 400 °C and 450 °C is observed due to the decomposition of CH ($Ca(OH)_2 \rightarrow CaO + H_2O$) – i.e., the second hump shown on the DSC curve (see Fig. 2 (a)), which is followed by a gradual mass loss as temperature increases to 675 °C (further loss of chemically bound water from C–S–H and the decomposition of $CaCO_3$). At 675 °C, most of the C–S–H decomposes, forms β-C_2S, and loses its binding capacity – i.e., third hump on the DSC curve. This transition is also signified by the XRD results shown in Fig. 2 (c), where a hump related to C–S–H was persistent up to 600 °C in x-ray diffraction data [30]. With further heat treatment up to 1150 °C, there was very little mass loss between 900 °C and 1150 °C.

The thermal decomposition process is further evidence by the X-ray diffraction (XRD) analysis conducted on paste specimens after exposure to high temperatures, see Fig. 2 (c). Main phases in the control specimen are identified as Portlandite (CH), C–S–H, and β-C_2S. Most of the peaks are persistent in samples with heat treatment at temperatures up to 400 °C. Mass loss between 105 °C and 400 °C shown in TGA, is not reflected by any identifiable phase change in x-ray diffractogram. This is consistent with observation made by Lim et al. [38]. A hump around $2\theta = 29.35$ related to C–S–H is persistent up to 400 °C, but disappears above 600 °C. This change is accompanied by an increase in intensity for peaks related to β-C_2S, which forms through C–S–H decomposition [39]. A reduction in peak intensity of CH is observed at 600 °C. This is consistent with the mass loss observed in TGA between 400 °C and 450 °C corresponds to decomposition of CH. It is noted that some peaks related to CH are still identified above 600 °C. This is likely due to incomplete decomposition of CH during heating, as well as the reformation of CH during cooling and sample storage [38].

Microstructurally, based on the multiscale nature of cementitious composites [2,3,40], the thermal deterioration of both calcium silicate hydrate (C–S–H) and calcium hydroxide (CH) solids is usually accompanied by the formation of micro-pores and cracks [38], see Fig. 3 (a). Fig. 3(b) presents the SEM images of polished LWCC specimens after exposure to elevated temperatures at 400 °C and 800 °C. The SEM images show that the LWCC specimen after exposure to 400 °C largely maintained the dense microstructure of cement paste (i.e., no noticeable roughness and porosity change was observed), in spite of the dehydration of C–S–H and associated mass loss. However, microcracks were observed on the sample heated to 400 °C and it seems that the cracks were originated from the interface between the paste matrix and inclusions (i.e., aggregates, mineral additives, or FAC). There is no observable gap between FAC and cement under this temperature. SEM investigation on specimens after exposure to 800 °C reveals that more microcracks were formed and an increase in roughness within the cement paste. The microstructure also appears to be more porous than that of the samples treated at lower temperatures. The microcracks become wider with increasing temperatures. The SEM images (Fig. 3 (b)) also show a clear gap around the FAC, which is likely caused by the irreversible shrinkage of cement paste. This observation is consistence with the SEM images shown in Huang et al. [31]. Its impact on the material's thermal and mechanical properties will be discussed in the following section.

2.3. Compressive strength

Following the heating program, mechanical tests were conducted using a MTS servo-hydraulic material testing system with a clamp-on extensometer for strain measurement, see Fig. 4 (a). The elastic modulus was tested according to ASTM C469 specifications, where the loading was carried out in displacement-controlled mode with the loading rate of 0.05 mm/min. Five cylindrical specimens from each group shown in Table 1 were tested for determining the elastic modulus and compressive strength.

The mechanical and physical properties tested for each specimen group are summarized in Table 3. Expectedly, elevated temperature led to gradual reductions in sample density – i.e., specimens exposed to 200 °C, 400 °C, 600 °C and 800 °C had mass losses of approximately 1.5–2%, 3.5%, 4.5%, 6%, respectively, as compared to the unheated reference specimen. The mass loss is mainly attributed to the evaporation of decomposed water from C–S–H, CH, and AFt because free water (capillary water) was removed before heating to the prescribed temperatures.

The compressive strength of LWCC reduces as the FAC volume fraction increases, and its dependence on the exposed temperature is plotted in Fig. 5 (a) and (b) showing ES106 and Es200/600 respectively. Significant reductions in compressive strength were observed for specimens exposed to 400 °C and above. At 600 °C, the compressive strength reductions for the reference mortar and the LWCCs having 7%, 14%, 21%, and 28% ES106 FAC are 67.3%, 59.3%, 55.7%, 52.3%, and 48.9%, respectively; and the corresponding reductions for LWCCs containing 7%, 14%, 21%, and 28% ES200/600 FAC are 74.1%,76.2%, 70.1%, and 64.0%, respectively. LWCCs containing smaller FAC particles (i.e., ES106) have higher compressive strength than those with larger FAC particles (ES200/600) in all temperature ranges. This is consistent with the authors' previous findings that hollow and core-shell fillers with smaller particle size (higher shell wall thickness to diameter ratio) and

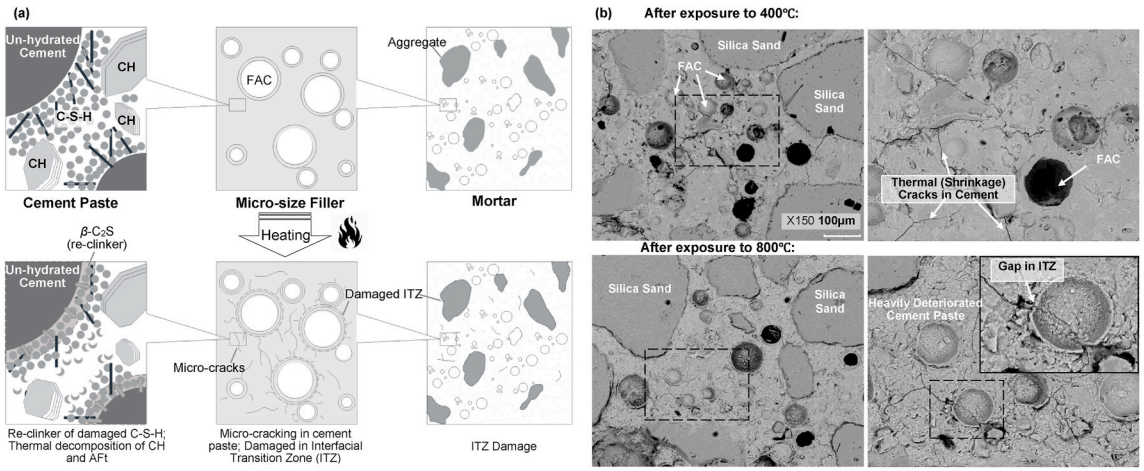

Fig. 3. Micro-structure evolution of compendious composites after exposed to elevated temperatures: (a) illustrative figure showing the micro-structure evaluation at different scales; and (b) SEM images showing the microstructure of cement composite mortar exposed to 400 °C and 800 °C.

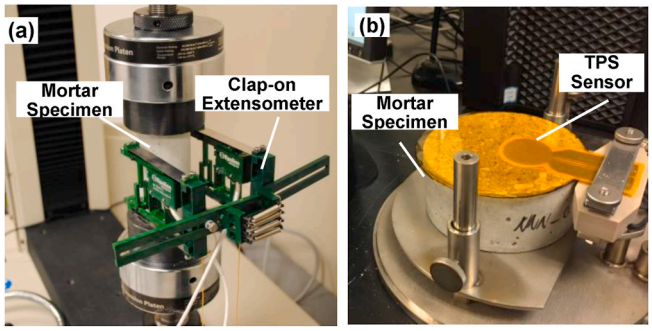

Fig. 4. Mechanical test setup: (a) setup of extensometers for elastic modulus measurement; and (b) setup for the transient plane source (TPS) test.

stiff shell help to improve the composites' mechanical performance by providing higher particle strength and stiffness [3,40]. The change of elastic moduli, as influenced by the properties of the inclusion phase (i.e., particle size, shell wall thickness etc.), under different exposed temperatures will be discussed in later sections along with modeling.

2.4. Thermal conductivity

The thermal constants of the control and heated specimens were tested through the transient plane source (TPS) method [41] using a *HotDisk TPS-1500* thermal constant analyzer [42], see Fig. 4 (b). In a TPS test, the transient temperature rises from a plane source (i.e., a Kapton supported double spiraled nickel metal sensor) that heats the surrounding material. By measuring the unbalanced voltage drops as a function of time, the thermal conductivity and thermal diffusivity of the tested material are simultaneously solved from one single transient recording through a process of iteration [43]. For the thermal conductivity measurements, three pairs of 50 mm diameter and 20 mm thick disc-shape mortar samples were used, see Fig. 4 (b).

Fig. 6 (a) and (b) present the change of thermal conductivity as a function of FAC volume fraction and exposure temperature for LWCC containing ES106 and ES200/600 FACs respectively. In general, the thermal conductivity (TC) of LWCC mortar decreases with the increase in FAC volume fraction. It should be mentioned that since the FACs were used to replace silica sand by its equivalent volume, the decrease in thermal conductivity as FAC volume fraction increases is attributed to both the inclusion of low conductivity FAC and the decreased volume fraction of silica sand. The thermal conductivity of LWCC is insensitive to the type and size of FAC used; rather, it is primarily controlled by its volume fraction. Fig. 6 also shows the temperature dependence of thermal conductivity, where the thermal conductivity generally starts to decrease even below 200 °C. The gradual decreasing of TC is primarily due to the thermal degradation of the cement paste phase – i.e., the loss of absorbed and physically bound water above 100 °C leads to the volume fraction change of hydration compounds and increase in micro-cracking. Below 400 °C, TC slowly decreases, mainly due to the loss of absorbed water. More drastic TC reduction was observed when temperatures above 400 °C. This is mainly attributed to the loss of physically bound water and the damage of interface transition zone (ITZ) between inclusion and cement paste. It is noted that the mortar samples having the least FAC concentration had the most significant TC change upon heating, which supports the observation that thermal degradation occurs mostly within the cement phase.

3. A multi-scale thermal degradation model to predict the elastic properties of cementitious composites exposed to elevated temperature

3.1. Model formulation

Fig. 7 presents the multiscale thermal degradation model using sub-stepping homogenization scheme for predicting the effective elastic and thermal properties of cementitious composites containing micro-size particulate inclusions (e.g., fly-ash cenospheres) after exposure to high temperature. Step 1 includes three parts – i.e., (a) thermal degradation (re-clinker) model for cement paste, (b) using effective medium theory to obtain the equivalent property of the inclusion phase, and (c) the spring-interface model to consider ITZ damage. For cement paste, the decomposed hydration products – i.e., CH, CaO product, unhydrated clinkers and re-clinkered product (β-C_2S), and capillary pores, coexist in cement paste after expose to elevated temperatures. The process is modeled using a thermal degradation model described in Jiang et al. [35]. The microcracks evolution during this process is captured by the model developed by Feng and Yu [44]. Then, the equivalent property of the micro-size core-shell particles is obtained by the equivalence model developed by the authors [40], also see Section 3.3. A 'spring-interface' model originally developed by Duan et al. [45] is employed to consider the ITZ damage as a function of the exposed temperature. Finally, Step 2 obtains the homogenized properties of cementitious composites using homogenization methods such as the Mori-Tanaka model.

3.2. Thermal degradation of cement paste

The decomposition of cement paste after exposure to elevated tem-

Table 3
Experimental results[a].

Mix ID	Heating Temp	Heated Density	Mass Loss	Elastic Modulus	Compressive Strength	Thermal Conductivity
	°C	kg/m^3	%	GPa	MPa	W/mK
Control	25	2093.77 ± 2.37	–	30.53 ± 0.74	92.77 ± 1.28	2.09 ± 0.01
	200	2050.22 ± 9.32	1.51%	29.02 ± 0.56	85.78 ± 4.50	2.00 ± 0.05
	400	2016.84 ± 8.90	3.60%	18.11 ± 1.10	58.63 ± 0.23	1.87 ± 0.04
	600	1980.19 ± 21.67	4.66%	2.43 ± 0.18	30.34 ± 0.69	1.34 ± 0.01
	800	1958.70 ± 4.86	6.06%	0.36 ± 0.08	10.75 ± 0.65	0.93 ± 0.02
ES106 7%	25	2001.92 ± 1.67	–	28.95 ± 0.82	103.36 ± 4.50	1.71 ± 0.01
	200	1959.92 ± 3.74	1.88%	25.55 ± 0.76	94.64 ± 0.72	1.57 ± 0.01
	400	1922.76 ± 2.15	3.90%	15.32 ± 1.16	66.01 ± 3.01	1.43 ± 0.01
	600	1890.41 ± 3.13	5.01%	2.79 ± 0.23	42.09 ± 0.29	1.17 ± 0.02
	800	1867.79 ± 18.46	6.66%	1.78 ± 0.08	22.09 ± 2.24	1.08 ± 0.02
ES106 14%	25	1783.81 ± 2.84	–	22.36 ± 1.29	85.56 ± 2.54	1.27 ± 0.01
	200	1756.25 ± 4.87	1.12%	20.40 ± 0.27	80.24 ± 2.38	1.20 ± 0.01
	400	1722.99 ± 6.94	3.53%	14.45 ± 0.41	61.28 ± 1.00	1.11 ± 0.01
	600	1705.36 ± 5.33	4.90%	3.90 ± 0.28	37.88 ± 1.02	0.93 ± 0.00
	800	1683.23 ± 9.33	5.06%	2.30 ± 0.08	24.26 ± 1.65	0.87 ± 0.00
ES106 21%	25	1650.62 ± 1.85	–	19.97 ± 0.52	80.87 ± 1.21	1.03 ± 0.02
	200	1616.00 ± 2.90	2.01%	16.99 ± 0.62	70.87 ± 5.11	0.96 ± 0.03
	400	1581.02 ± 5.02	4.26%	11.42 ± 0.45	55.00 ± 2.88	0.90 ± 0.01
	600	1569.48 ± 4.94	5.66%	3.65 ± 0.22	38.59 ± 0.69	0.73 ± 0.02
	800	1548.64 ± 11.86	6.64%	2.66 ± 0.21	24.63 ± 3.36	0.70 ± 0.01
ES106 28%	25	1532.68 ± 3.01	–	17.33 ± 0.65	78.36 ± 0.28	0.85 ± 0.01
	200	1497.01 ± 4.07	2.37%	14.56 ± 1.18	68.50 ± 2.69	0.78 ± 0.01
	400	1462.88 ± 3.78	4.92%	9.71 ± 0.79	54.90 ± 1.63	0.67 ± 0.01
	600	1448.41 ± 6.26	6.38%	4.07 ± 0.05	40.07 ± 1.04	0.59 ± 0.00
	800	1420.23 ± 6.81	7.20%	3.09 ± 0.09	27.85 ± 2.24	0.60 ± 0.00
ES200/600 7%	25	1928.21 ± 2.03	–	26.40 ± 0.77	84.09 ± 2.74	1.76 ± 0.02
	200	1905.29 ± 3.71	1.51%	21.10 ± 0.83	70.99 ± 2.79	1.65 ± 0.01
	400	1867.25 ± 5.87	2.86%	1.16 ± 0.96	42.70 ± 2.65	1.54 ± 0.03
	600	1844.72 ± 6.64	4.38%	1.63 ± 0.23	21.78 ± 1.11	1.03 ± 0.02
	800	1812.74 ± 63.15	6.12%	0.63 ± 0.03	7.25 ± 0.45	0.82 ± 0.01
ES200/600 14%	25	1761.01 ± 2.26	–	24.71 ± 0.87	80.17 ± 0.91	1.40 ± 0.00
	200	1749.18 ± 8.50	0.95%	17.91 ± 0.59	61.40 ± 0.37	1.34 ± 0.02
	400	1725.65 ± 10.95	2.88%	9.44 ± 0.67	39.77 ± 2.09	1.17 ± 0.01
	600	1688.76 ± 7.42	4.23%	1.62 ± 0.15	19.10 ± 0.39	0.84 ± 0.01
	800	1650.16 ± 2.53	6.65%	0.95 ± 0.05	10.88 ± 0.57	0.75 ± 0.03
ES200/600 21%	25	1700.52 ± 3.30	–	20.65 ± 1.27	70.69 ± 2.03	1.27 ± 0.01
	200	1666.97 ± 3.25	1.70%	14.83 ± 0.65	58.55 ± 1.15	1.19 ± 0.00
	400	1648.36 ± 6.32	2.83%	7.74 ± 1.10	29.29 ± 2.14	0.96 ± 0.02
	600	1618.22 ± 3.97	5.09%	1.82 ± 0.03	21.15 ± 0.66	0.68 ± 0.01
	800	1583.54 ± 4.87	6.65%	1.09 ± 0.01	11.85 ± 0.35	0.61 ± 0.00
ES200/600 28%	25	1556.27 ± 3.57	–	16.86 ± 0.53	60.33 ± 2.97	1.03 ± 0.01
	200	1513.68 ± 5.72	2.03%	12.34 ± 0.29	52.71 ± 2.09	0.93 ± 0.01
	400	1480.91 ± 17.62	3.73%	6.51 ± 0.17	38.07 ± 0.11	0.76 ± 0.02
	600	1466.94 ± 5.77	4.98%	1.95 ± 0.08	21.74 ± 0.60	0.56 ± 0.00
	800	1438.16 ± 5.96	7.52%	1.31 ± 0.04	12.21 ± 0.59	0.57 ± 0.03

[a] Results are presented as the statistical average of measurements on five specimens. The stand deviations are shown as error bars in Figs. 5–6.

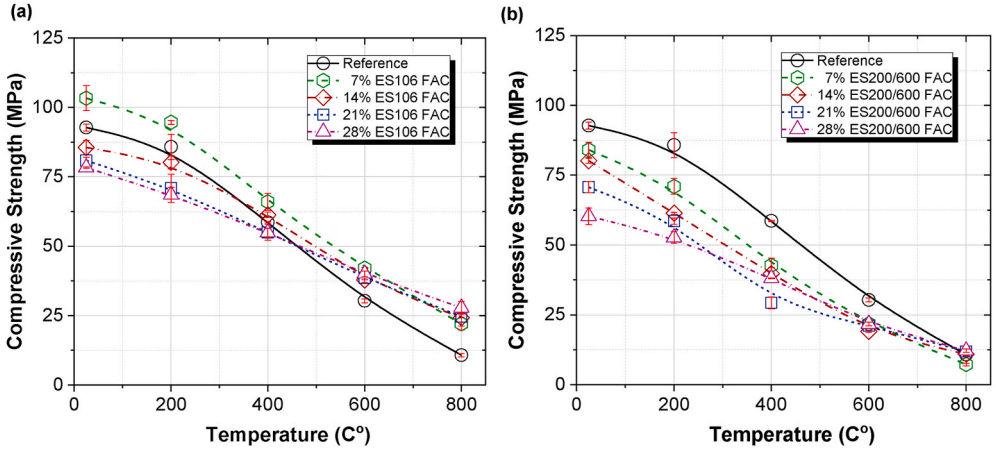

Fig. 5. Relationship between compressive strength with FAC volume fraction and exposure temperature for (a) LWCCs containing ES106 FAC; and (b) LWCCs containing ES200/600 FAC.

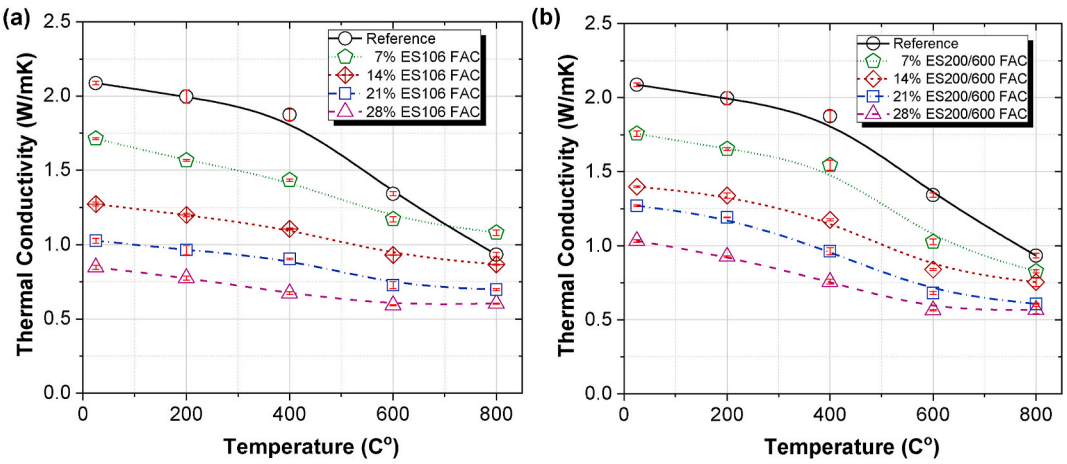

Fig. 6. Thermal conductivities obtained through Transient Plane Source (TPS) method for: (a) LCC containing ES106 FAC; and (b) ES200/600.

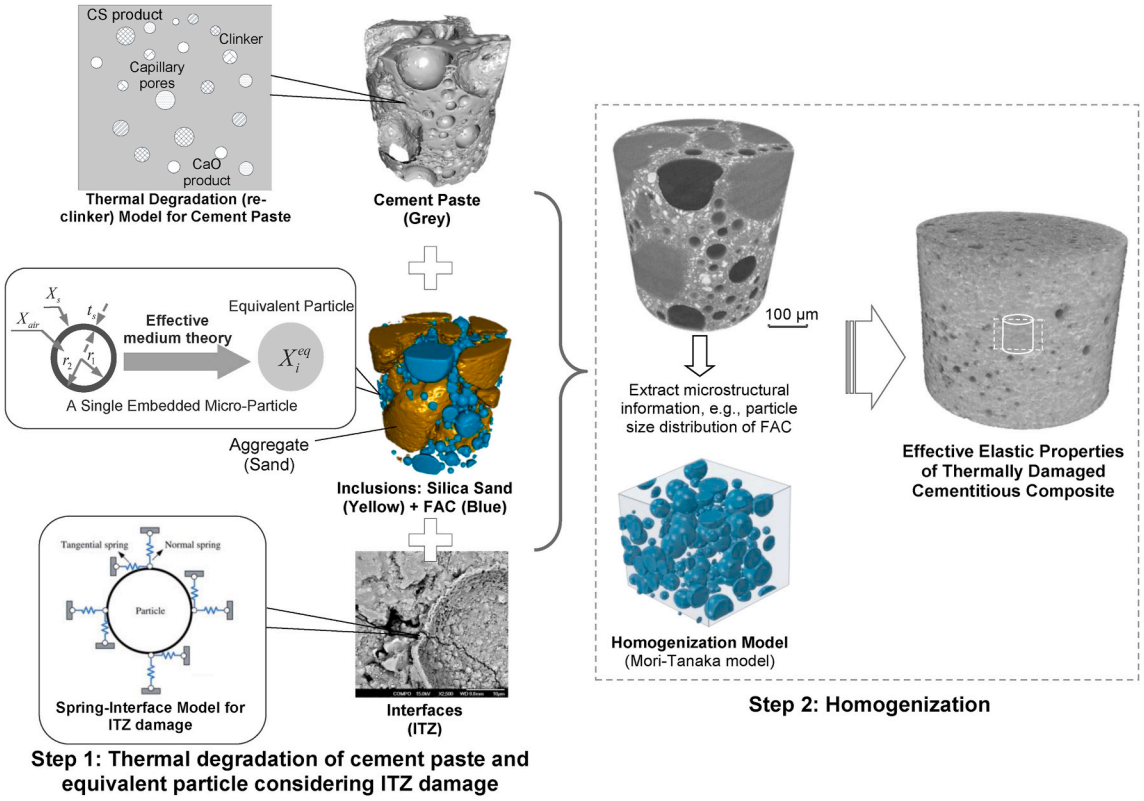

Fig. 7. A multiscale thermal degradation model using sub-stepping homogenization scheme for predicting the effective elastic modulus of cementitious composites containing micro-size functional fillers after exposure to high temperature.

perature is estimated by the method proposed by Zhao et al. [33,34] and Jiang et al. [35]. Given the cement type, water to cement ratio (w/c) and curing time, the degree of hydration, a_c, is estimated by the model of hydration developed by Parrot and Killoh [46] and Lothenbach et al. [47]. The hydration of cement is composed by the processes of nucleation, diffusion, and the formation of a hydration shell of cement and the degree of hydration is controlled by the slowest rate of hydration of the three processes. For a specific cement type, the degree of hydration for each clinker phase (i.e., C_3S, C_2S, C_3A, and C_4AF) can be calculated as a function of time. Then, the degree of hydration of cement, a_c, is calculated as a weighted average of the degrees of hydration of the clinker phases.

3.2.1. *Thermal degradation of cement paste*

Fig. 8 presents the procedure of calculating the constituents of cement paste before and after exposure to high temperature. With the degree of hydration, the volume fractions of unhydrated cement, φ^0_{unhyC}, and hydrated cement gel, φ^0_{gel}, in hardened cement paste are calculated by Ref. [33]:

$$\varphi^0_{unhyC} = \frac{0.32(1-a_c)}{w/c+0.32} \tag{1}$$

$$\varphi^0_{gel} = \frac{0.68a_c}{w/c+0.32} \tag{2}$$

Cement gel as the hydrated products of cement is mainly composed

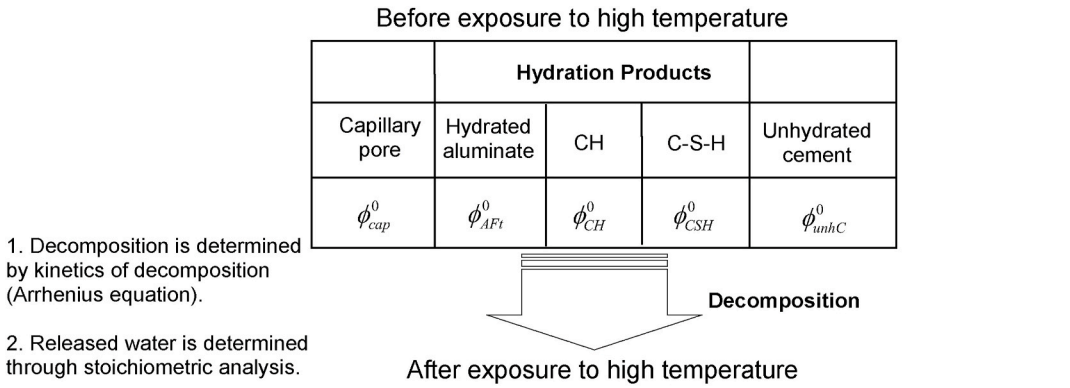

Fig. 8. Constituents of cement paste before and after exposed to high temperature.

of C–S–H, CH, and hydrated aluminates (AFt). The volume fractions of C–S–H, CH, and AFt in cement gel are obtained by the reaction volume stoichiometry developed by Bentz and Garboczi [48], where each volume unit of C_3S produces 1.7 vol units of C–S–H and 0.61 vol units of CH; each volume unit of C_2S produces 2.39 vol units of C–S–H and 0.191 vol units of CH, and each volume unit of both C_3A and C_4AF produce 1.69 vol units of hydrated aluminates.

After exposure to elevated temperature, C–S–H, CH, and AFt start to decompose at different initiation temperatures as depicted in the previous section. The decomposed volume fractions of the ith constituent, φ_i^d, can be expressed as a function of their corresponding initial volume fractions, i.e.,

$$\varphi_i^d = a_i \varphi_i^0 \tag{3}$$

where, a_i is the conversion degree of the ith constituent (i = C–S–H, CH, and AFt) as a function of temperature. The rate of conversion degree, da_i/dt, of the ith constituent is determined by the reaction kinetics as [35]:

$$\frac{da_i}{dt} = A_i \exp\left(-\frac{E_{a,i}}{R(T(t)+273.15)}\right) f_i(a_i)\left(H_V\left(a_{eq,i}-a_i\right)H_V\left(T(t)-T_{onset,i}\right)\right) \tag{4}$$

where, A_i, $E_{a,i}$, $f(a_i)$, $a_{eq,i}$, and $T_{onset,i}$ are the pre-exponential factor, activation energy, reaction model, equilibrium conversion degree, and conversion onset temperature for the ith constituent respectively; R, T, and t are the universal gas constant, temperature in degree of Celsius, and time in seconds, respectively; and $H_V(\cdot)$ is the Heaviside step function. The parameters in Equation (4) for C–S–H, CH, and AFt are adopted from Jiang et al. [35] and are listed in Table 4.

Given the temperature history, $T(t)$, the conversion degree of each constituent i can be calculated by a simple incremental method:

$$a_i(t+\Delta t) = a_i(t) + \dot{a}_i(t)(\Delta t) \tag{5}$$

The water released from the reactants is regarded as additional pores and its volume fraction φ_i^p is given by Ref. [33]:

$$\varphi_i^p = \varphi_i^d n_i^w \frac{\rho_i/M_i}{\rho_w/M_w} \tag{6}$$

where, n_i^w is the amount of water in mole decomposed per mole of reactant i, ρ_i, M_i, and ρ_w, M_w are the density and mole mass of reactant i and water, respectively. Table 5 summarizes the parameters of Equation (6) based on the stoichiometric analysis performed by Zhao et al. [33].

Table 5
Parameters to calculate volume fractions of water from reactants decomposition.

Reactant	n_i^w (–)	ρ_i (g/cm^3)	M_i g/mol	φ_i^p (–)
Water	–	1.00	18.02	–
C–S–H	3.0	1.75	365	0.69
CH	1.0	2.24	74	0.54
AFt	20	1.80	1255	0.52

Table 4
Parameter for kinetics of hydrates decomposition in hardened cement pastes [35].

Substance	$T_{onset,i}$ °C	A_i (1/s)	$E_{a,i}$ (kJ/mol)	$f_i(a_i)$	$a_{eq,i}$
C–S–H	110	$0 \le a \le 0.8$, $A = \exp\begin{pmatrix}1038.56a^5 - 1914.27a^4 + 1250.96a^3 \\ -404.32a^2 + 95.17a + 7.08\end{pmatrix}$ $0.8 < a \le 1$, $A = \exp(133.17a - 85.36)$	$0 \le a \le 0.8$, $E_a = 205.24a + 69.08$ $0.8 < a \le 1$, $E_a = 1395.99a - 883.53$	$f(a) = 1 - a$	$a_{eq} = 1 - \exp(-0.658(T - T_{onset})^{0.252})$
CH	430	$A = 7.58 \times 10^6$	$E_a = 127$	$0 \le a \le 0.5$, $f(a) = 2a^{0.5}$ $0.5 < a \le 1$, $f(a) = 2(1-a)^{0.5}$	$a_{eq} = 1$
AFt	70	$A = 1.67 \times 10^4$	$E_a = 59$	$f(a) = (1-a)^{0.5}$	$a_{eq} = 1$

3.2.2. Elastic moduli of thermally damaged cement paste

The effective elastic moduli of cement paste after exposure to high temperature can be treated as a composite system using a micromechanics-based model, where the undecomposed cement paste is modeled as the matrix and the decomposed products are added as inclusions. The solid packing density of the decomposed hydration products are typically smaller than 50% (i.e., porosities greater than 50%, see Table 5). According to granular mechanics, the stiffness of a granular assembly is negligible when its packing density is lower than the random loose packing limit of 56% [49]. Therefore, the elastic modulus of cement paste after exposed to high temperature, $E_{m,t}$, can be estimated using the three-phase model by assuming the Poisson's ratio does not change before and after exposure to high temperature [50]:

$$E_{m,t} = E_{m,0} - \frac{\varphi_m^d E_{m,0}}{1 - 3\left(1-\varphi_m^d\right)E_{m,0}\Big/\left(3E_{m,0}+4\mu_{m,0}\right)} \tag{7}$$

where $\varphi_m^d = \sum \varphi_i^d$ is the volume fraction of the decomposed hydration products, see Fig. 7; $K_{m,0}$ and $\mu_{m,0}$ are the bulk and shear moduli of the cement paste at room temperature respectively. The undecomposed hydration products are assumed to be the matrix and their decomposed counterparts are treated as voids in the cement paste composite system.

To consider the microcracks developed in cement paste during the heating process (Fig. 7), the model developed by Feng and Yu [44] is adopted. Assuming the microcracks are uniformly distributed and orientated, the elastic modulus of thermal damaged cement paste with microcracks can be written as [44]:

$$E_{m,t}^c = \frac{E_{m,t}}{1 + g(\nu_{dil})\omega\left[1 + g\left(\nu_{m,t}\right)\omega\right]} \tag{8}$$

where $\nu_{dil} = \frac{\nu_{m,t}}{[1+g(\nu_{m,t})\omega]}\left(1 + \frac{g(\nu_{m,t})\omega}{(10-3\nu_{m,t})}\right)$, and $g(x) = \frac{16(1-x^2)(10-3x)}{45(2-x)}$, and ω is the microcrack density parameter, which can be determined through experimental calibration [33]. Although there are some efforts [51,52] in trying to understand the relationship between microcrack density and elevated temperature, there still lacks a systematic methodology to quantify such a relationship. In this study, ω is determined to be 0, 0.054, 0.27, and 0.45 for temperature at 200 °C, 300 °C, 450 °C, and 600 °C respectively. For temperature below 600 °C, ω is obtained through interpolation between the neighboring given temperatures. For temperature above 600 °C, ω is assumed to be equal to the value at 600 °C.

3.3. Elastic properties of the inclusion phase

For inclusions with a hollow or core-shell configuration, such as fly-ash cenospheres FAC, it can be considered as a solid particle having the same dimension with equivalent elastic properties, see Fig. 7. The equivalent elastic properties can be established through Eshelby's strain energy equivalence [53], and the equivalent bulk modulus of the inclusion, K_I^{eq}, is obtained as [50]:

$$K_I^{eq} = K_s + \frac{(K_c - K_s)p}{1 + (1-p)\left[(K_c - K_s)\Big/\left(K_s + 4/3\mu_s\right)\right]} \tag{9}$$

where $p = (r_1/r_2)^3$ is the volumetric ratio of the core in a core-shell particle, see Fig. 7; K_s, μ_s, and K_c, μ_c are the bulk and shear moduli of the shell and core materials, respectively.

The equivalent shear modulus of a core-shell particle, μ_I^{eq}, is obtained by solving:

$$A_1\left(\frac{\mu_I^{eq}}{\mu_s}\right)^2 + A_2\left(\frac{\mu_I^{eq}}{\mu_s}\right) + A_3 = 0 \tag{10}$$

where coefficients A_1, A_2, and A_3 are the functions of the core/shell material elastic properties and the volumetric ratio of the core p. The formulations of A_1, A_2, and A_3 can be found in a previous paper of the authors [40].

After exposure to temperature higher than 650 °C, surface morphology change was observed for FACs (Fig. 2), indicating certain levels of thermal damage. However, since both FAC and silica sand are mostly thermally stable under 800 °C, the change of their mechanical properties are negligible when compared with the elastic property degradation caused by the damage of the ITZ at temperatures above 400 °C [15]. Therefore, the thermal degradation of the inclusions is not explicitly modeled; instead, its effect is implicitly considered in the damage of ITZ through the spring-interface model as described in the next section.

3.4. Equivalent inclusion properties considering ITZ damage

For the equivalent particle elastic properties considering interfacial damage, the linear spring-interface model (LSM) originally developed by Duan et al. [45] is adopted. The LSM assumes continuity of stress and discontinuity of displacement (displacement jump) at the boundary between the matrix and embedded inclusions. The displacement jump is assumed to be equal to the displacement of normal and shear linear springs as shown in Fig. 7. Based on the principal of energy equivalence, the equivalent particle elastic properties with interfacial damage can be written as [45]:

$$K_{I,d}^{eq} = \frac{K_I^{eq}}{1 + 3\beta_n' K_I^{eq}} \tag{11}$$

$$\mu_{I,d}^{eq} = \mu_I^{eq}\frac{c_1 + 8\mu_I^{eq}(7+5\nu_I^{eq})\left(2\beta_s' + 3\beta_n'\right)}{c_1 + 2\mu_I^{eq}\beta_s' c_2 + 2\mu_I^{eq}\beta_n'(3c_2 - c_1) + 80(\mu_I^{eq})^2(7+5\nu_I^{eq})\beta_s'\beta_n'} \tag{12}$$

where $c_1 = 20(7 - 10\nu_I^{eq}) + 5\frac{\mu_I^{eq}}{\mu_m}(7 + 5\nu_I^{eq})$, $c_2 = 20(7 - 4\nu_I^{eq}) + 3\frac{\mu_I^{eq}}{\mu_m}(7 + 5\nu_I^{eq})$, $K_{I,d}^{eq}$ and $\mu_{I,d}^{eq}$ are the bulk and shear modulus of the equivalent particle considering interfacial damage respectively; β_s' and β_n' are the interfacial compliance parameters in tangential and normal directions respectively. It is clear that β_s' and β_n' control the damage of the interface; where β_s' and β_n' equal to zero represent perfect interface and while approaching to infinity indicates interface debonding. The thermal damage evolution of the interface as a function temperature is expressed as [32]:

$$\beta_n' = b_0 \tan(b_1 \Delta T) \tag{13a}$$

$$\beta_s' = b_2 \tan(b_3 \Delta T) \tag{13b}$$

where ΔT is the temperature increment; and the coefficients b_0, b_1, b_2, and b_4 can be determined based on experimental results.

3.5. Homogenization

With the elastic properties of the thermally degraded cement paste and the equivalent inclusion determined following the previous sections, the effective properties of cementitious composites after exposure to high temperature can be estimated using Mori-Tanaka method [54]. The effective elastic tensor, $\overline{\mathbf{C}}$, of a composite system containing N inclusions (the jth) may be estimated as:

$$\overline{\mathbf{C}} = \mathbf{C}_m + \sum_{j=1}^{N} \varphi_j\left(\mathbf{C}_{I,j} - \mathbf{C}_m\right)\mathbf{\Gamma}^{\mathrm{C}}_{(\mathrm{MT}),j} \tag{14}$$

where φ_j is the volume fraction of the jth inclusion; $\mathbf{C}_{I,j}$ and $\mathbf{C}_m$ are the elastic tensors of the jth inclusion and the matrix, respectively; and

$\mathbf{\Gamma}^{C}_{(MT),j}$ is the Mori-Tanaka strain concentration tensor of the jth inclusion:

$$\mathbf{\Gamma}^{C}_{(MT),j} = \left[\varphi_j \mathbf{I} + \varphi_m \left(\mathbf{\Gamma}^{C}_{dil,j}\right)^{-1} + \sum_{l=1}^{N} \varphi_l \mathbf{\Gamma}^{C}_{dil,l} \left(\mathbf{\Gamma}^{C}_{dil,j}\right)^{-1}\right]^{-1}, \quad l \neq j \tag{15}$$

where $\mathbf{I}$ is a fourth order identity tensor, φ_m is the volume fraction of the matrix, and $\mathbf{\Gamma}^{C}_{dil,j}$ is the strain concentration tensor of the jth inclusion under the dilute scheme [54]:

$$\mathbf{\Gamma}^{C}_{dil,j} = \left[\mathbf{I} + \mathbf{S}^{C}_{m} \mathbf{C}_{m}{}^{-1} \left(\mathbf{C}_{I,j} - \mathbf{C}_{m}\right)\right]^{-1} \tag{16}$$

where $\mathbf{S}^{C}_{m}$ is the Eshelby's tensor, which can be found in Ref. [53].

4. Results and discussion

4.1. Evolution of elastic moduli after exposure to elevated temperature: model validation

The elastic moduli of cementitious composites containing fly-ash cenospheres (FACs) after exposure to elevated temperature is predicted using the thermal degradation model presented in Section 3 with the materials properties given in Table 6. The predicted and experimentally measured elastic moduli are plotted in Fig. 9 (a) and (b) showing ES106 and ES200/600, respectively. The elastic moduli predicted by the model are generally in good agreement with the corresponding experimental results. Similar to the trend of compressive strength, significant elastic modulus loss was observed between 200 °C and 600 °C for LWCCs containing ES106 and ES200/600 FACs. The degradation rate of mechanical properties is higher for LWCC mixtures having lower FAC volume fractions. This is likely due to two factors: 1) the thermal degradation mainly originated from cement past and within ITZ; and 2) the interfacial thermal deterioration between silica sand and cement matrix initiates at lower temperatures as compared to that between FAC and cement paste. The degradation of the ITZ after exposure to elevated temperatures will be discussed in greater details in the following section. At 600 °C, the residual elastic moduli of LWCCs with different volume fractions became close to each other around 1.5–3.5 GPa. The change of the elastic modulus between 600 °C and 800 °C was minimal.

Compared with LWCCs containing ES106 FAC, the elastic moduli of LWCCs containing ES200/600 FAC are slightly lower at room temperature and under elevated temperatures. At room temperature, this is mainly due to the smaller shell wall thickness to D_{50} ratio ($2t_s/D_{50}$) of ES200/600 FAC (t_s = 18 μm, D50 = 335.6 μm), in comparison with the $2t_s/D_{50}$ for ES106 FAC (t_s = 8.38 μm, D50 = 78.5), which are 0.21 for ES106 and 0.11 for ES200/600, respectively. This trend tends to diminish after exposure to 600 °C and above, at which point the cement paste and ITZ are severally damaged causing the inclusion phase losing bonding with the matrix.

Table 6
Constituents properties for cementitious composites containing FACs.

Properties	Cement paste	Silica sand	Shell of FAC	Core of FAC
Elastic modulus (GPa)	32	72	28	1.0×10^{-4}
Poisson's ratio (–)	0.25	0.17	0.21	0
Coefficient of thermal expansion[a] (/°C)	14.4×10^{-6}	10.4×10^{-6}	6.45×10^{-6}	–

[a] The coefficients of thermal expansion are measured at room temperature (25 °C).

4.2. Deterioration of cement paste under elevated temperatures

The conversion degree of the hydration products at elevated temperatures, which can be calculated using Equation (4), are presented in Fig. 10 (a) – (c). Three different heating rates, i.e., 0.5 °C/min, 5 °C/min, and 30 °C/min, are presented to show the effect of heating rate on the conversion degrees of AFt, C–S–H, and CH up to 800 °C, together with the equilibrium conversion degree at various temperatures. It can be seen that at 0.5 °C/min (the experimental heating rate adopted in this study), both AFt and CH reached their equilibrium state (completely decomposed) when reaching 800 °C; whereas for C–S–H the conversion degree did not fully reach the equilibrium state when first reaching 800 °C, but with the 3-hr holding time at 800 °C, C–S–H also reached the equilibrium – the holding time needed for C–S–H to reach equilibrium state at 800 °C is 38 min with the heating rates of 0.5 °C/min. It is noted that the time required for C–S–H decomposition to reach equilibrium is highly dependent on temperature – e.g., at lower target temperatures it takes long time for C–S–H to reach equilibrium which explains the difference between the simulated curve and the 'equilibrium state' curve presented in Fig. 10 (b). In addition, the effects of the decomposition of hydration products and microcracking on the elastic modulus of cement paste are plotted in Fig. 10 (d) – micro-cracking starts to take effect at temperatures exceeding 200 °C as represented by the model. It is worthwhile to mention that the formation of microcracks in cement-based materials is complex and may require future research.

4.3. Thermal damage of interfacial transition zone (ITZ)

As revealed by the studies conducted by Lim et al. [38], during the heating process C–S–H exhibits shrinkage due to moisture loss which is an irreversible process – i.e., it does not regain its original volume upon cooling, as shown in Fig. 11 (a), whereas aggregates and the micro-size FAC fillers expand during the heating process and may occupy the space created by shrinkage of cement paste. The thermal expansion of aggregates and FAC, however, is expected to be reversible. Therefore, contraction of aggregates and FAC filler during the cooling process is not accompanied by a regain of the original volume of cement paste, which leaves a gap at the interface, see Fig. 11 (a). On the other hand, the interface hydration products, mainly composed of ettringite and C–S–H, decompose at elevated temperatures. In this study, the ITZ between silica sand and cement paste experienced more severe damage than that between FAC and cement paste. This is mainly due to the higher level of coefficient of thermal expansion mismatch between silica sand and cement paste and that the interface hydration products are mainly composed by ettringite which decomposes at a relatively low temperature; whereas the pozzolanic reactivity of FAC promotes formation of the C–S–H gel at the interface [2]. Therefore, the interface damage parameter of silica sand was set to a larger value than the FAC's. It also worthwhile to note that silica sand usually has an irregular shape which may reduce the effect of interfacial damage to the elastic modulus of cementitious composites through boundary interlocking and friction [55], and therefore making the predicted results slightly lower than experimental results, see Fig. 9.

The interface damage is considered in the multiscale thermal degradation model through Equations (11) – (13). The values of the interface damage parameters used in this study for silica sand, ES106 FAC and ES200/600 FAC are listed in Table 7. It is noted that the values of the interface damage parameters are within the range suggested by Zhang et al. [32] - the interfacial damage parameters in the tangential direction can be assumed to have the same values as those in the normal direction and the value of b_0/b_2 (tangential direction) is between 0 and 0.1, and the value of b_1/b_3 (normal direction) is between $\pi/2000$ and $\pi/1200$. Fig. 11 (b) and (c) present the degree of interface damage calculated as a function of temperature for each inclusion type and their corresponding equivalent particle elastic modulus considering interface damage, where the degree of interface damage is defined as the value of

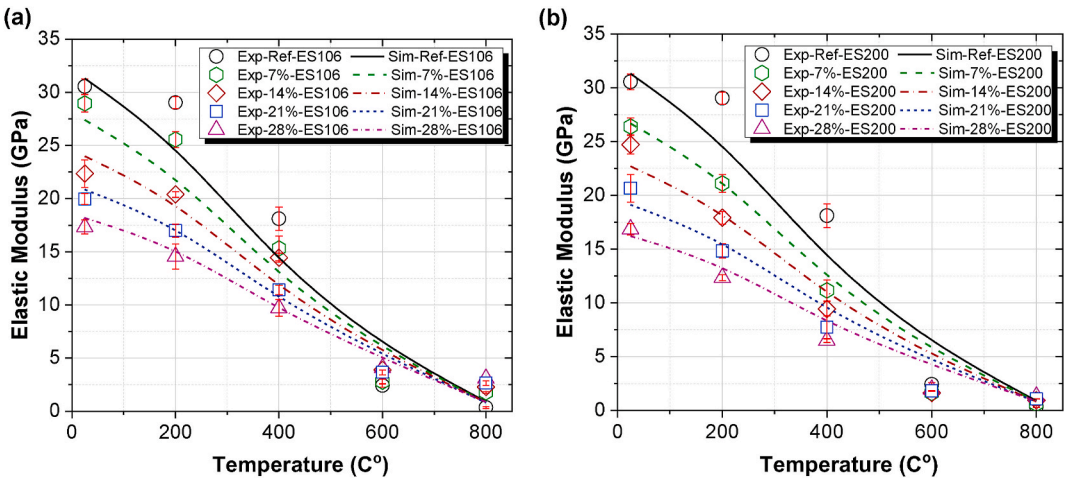

Fig. 9. Predicted and measured elastic modulus of LWCC with different FAC volume fractions: (a) LWCCs containing ES106 FAC; and (b) LWCCs containing ES200/600 FAC.

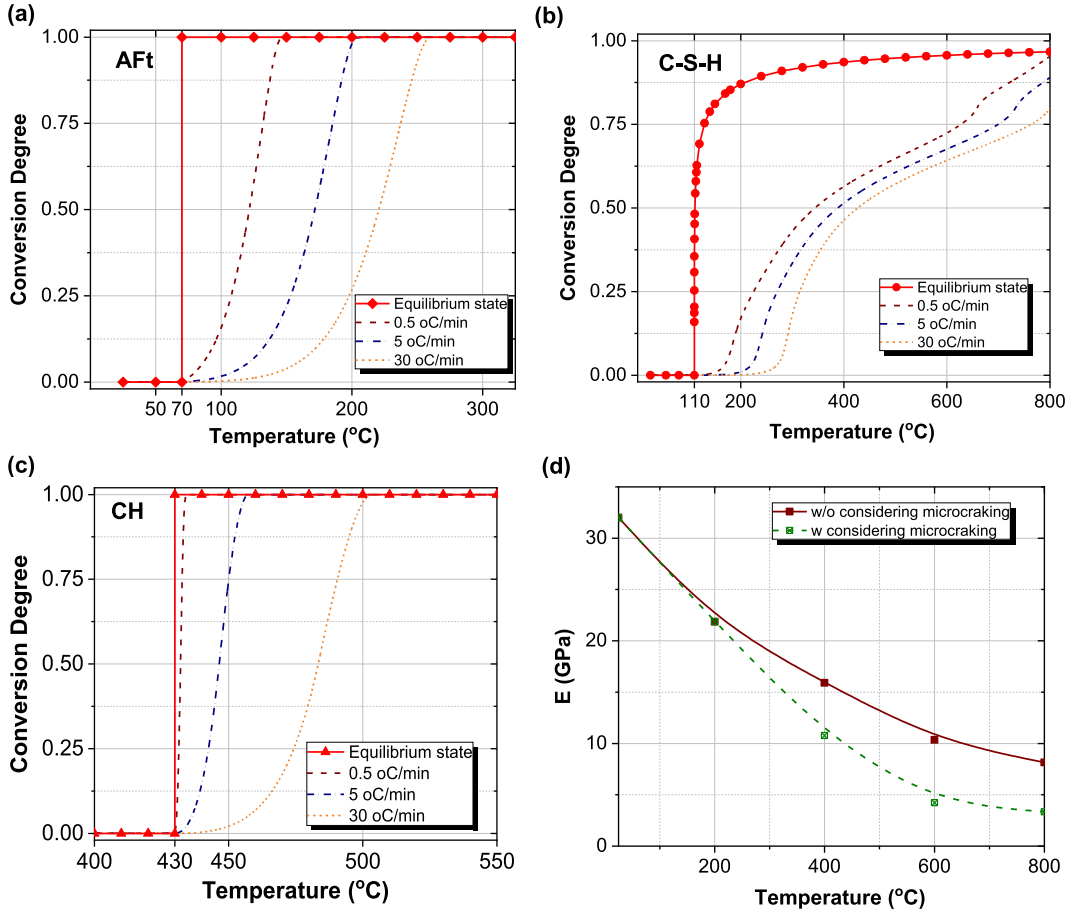

Fig. 10. Effects of heating rates on conversion degree for: (a) AFt; (b) C–S–H; and (c) CH; and (d) elastic modulus of cement paste with/without considering microcracking.

interface damage at a given temperature. As expected, the interface damage of silica sand (inclusion with high stiffness) leads to a higher level of elastic modulus loss than the FACs (soft inclusion), see Fig. 11 (c).

4.4. Effects of FAC size and volume fraction

Fig. 12 shows the effects of FAC type (size) and exposure temperature on concrete density (a), thermal (b), and mechanical properties (c) and (d). The densities of LWCC with two types of FAC are similar and the weight losses due to heating are mostly under 5% for both materials. In general, the thermal conductivity (TC) of LWCC containing ES106 FAC is approximately 10% lower than that of LWCC with ES200/600 FAC. However, this trend reversed for materials that were exposed to 600 °C and above. This is believed to be caused by the micro-thermal cracking at the FAC-cement matrix interface (ITZ around FAC particles) – i.e.,

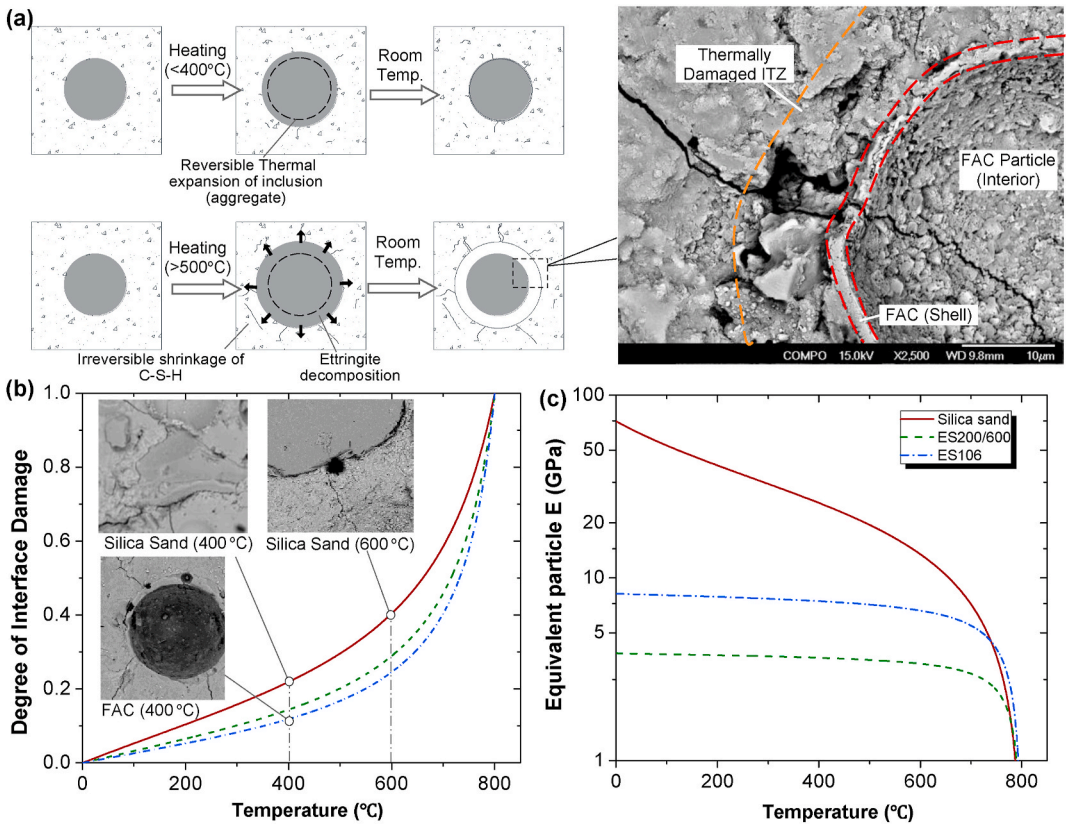

Fig. 11. Interface thermal damage and particle equivalent properties: (a) illustrative figure showing the interface damage after exposure to elevated temperature; (b) degree of interface damage; and (c) equivalent particle elastic modulus of silica sand, ES200/600, and ES106 FAC as functions of temperature.

Table 7
Interface damage parameter for different inclusions.

Parameters	Silica sand	ES106 FAC	ES200/600 FAC
b_0	0.025	0.012	0.015
b_1	1600/π	1600/π	1600/π

LWCC with smaller size fillers (e.g., ES106 FAC) has greater accumulative matrix-particle interface area, which leads to higher chance of thermal cracking in the ITZ region. Overall, LWCC with smaller FAC has notably better mechanical properties (elastic modulus and compressive strength) than its counterpart with larger size FAC filler with same FAC volume fraction and exposure temperature (also see Fig. 13). This is consistent with the authors' previous studies [2,3] and the trend holds for all temperature ranges. However, it is noted that the elastic modulus and compressive strength deteriorates at higher rate for LWCC with ES106 as exposure temperature increases, which is likely due to the same reason as the change of TC – i.e., greater ITZ area leads to higher micro-crack density when exposed to high temperature. Interestingly, at temperatures above 600 °C LWCC samples with ES106 FACs show better mechanical performance than that of the reference group without FAC.

Moreover, Fig. 13 presents the effect of FAC volume fractions on the elastic modulus of LWCCs after exposure to high temperatures. Generally, increasing the volume fraction of FACs leads to the decrease of the elastic modulus of LWCCs because they have lower equivalent elastic modulus than cement paste and silica sand, see Table 6 and Fig. 11 (c). At room temperature (RT), increasing the volume fraction of FAC from 0 to 0.45 leads to 56% and 63% elastic modulus reduction for LWCCs containing FAC ES106 and ES200/600, respectively. The comparison between experimental data and simulation results presented in Figs. 9 and 13 show good agreements between the model developed in this paper and experimental observations, both for predicting the elastic property evolution of cementitious composites containing different concentrations of filler particles (Fig. 13), as well as for the exposure to various temperatures (Fig. 9). It is noted that for cement composites exposed to higher temperatures (i.e., 600 °C and above), increasing in filler concentration has little effects on the composites' elastic moduli. This is consistent with experimental observations that after exposure to higher temperatures, the elastic properties of the composite system are dominated by severe damage in the cement matrix and within the ITZ.

5. Conclusions

This paper investigates the multi-scale thermal degradation of cementitious composites after exposure to elevated temperatures. The thermal degradation of cementitious composites containing functional inclusions is generally attributed to the damage of the cement paste caused by thermal decomposition and thermal incompatibility, the deterioration of aggregates and inclusion phases, and the interfacial damage between the inclusions and the matrix. To understand these phenomena, experiments were carried out both at micro- and macro-scale, where a series of lightweight cementitious composites containing fly-ash cenospheres (FAC) with various particle sizes and concentrations were made. Macroscopic level properties including mechanical (elastic moduli and compressive strengths) and thermal properties were measured as functions of the exposure temperature up to 800 °C. Simultaneous DSC-TGA, X-ray diffraction, X-ray fluorescence, and microscopy studies were employed to investigate the thermal degradation mechanism at multiple scale, including the thermal decomposition and microcracking of cement paste, the thermal deterioration of inclusions, and the thermal damage within the interfacial transition zone (ITZ). Based on the experimental observations, a multiscale thermal degradation model using a sub-stepping homogenization scheme was developed where two levels of core-shell particle (CSP) filled cement composite

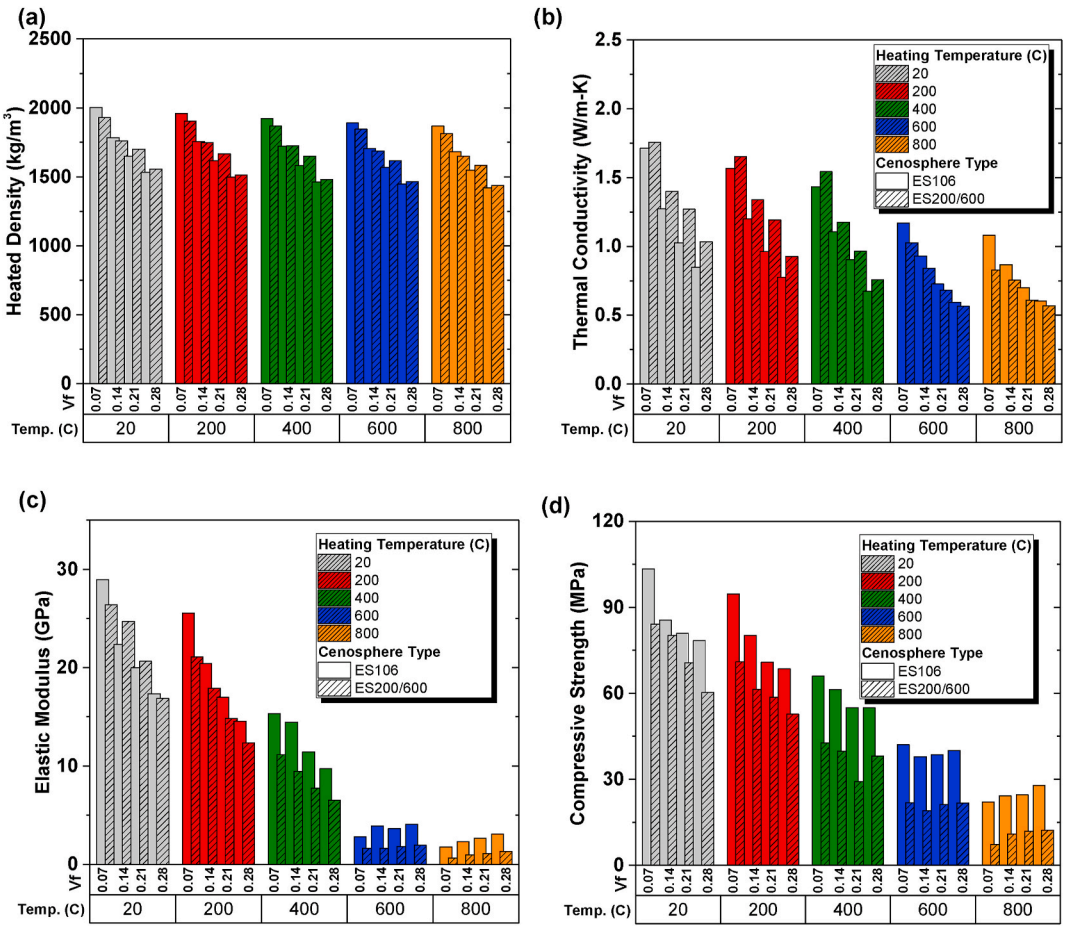

Fig. 12. Effect of FAC size and volume fraction on (a) oven-dry density; (b) thermal conductivity; (c) elastic modulus; and (d) compressive strength.

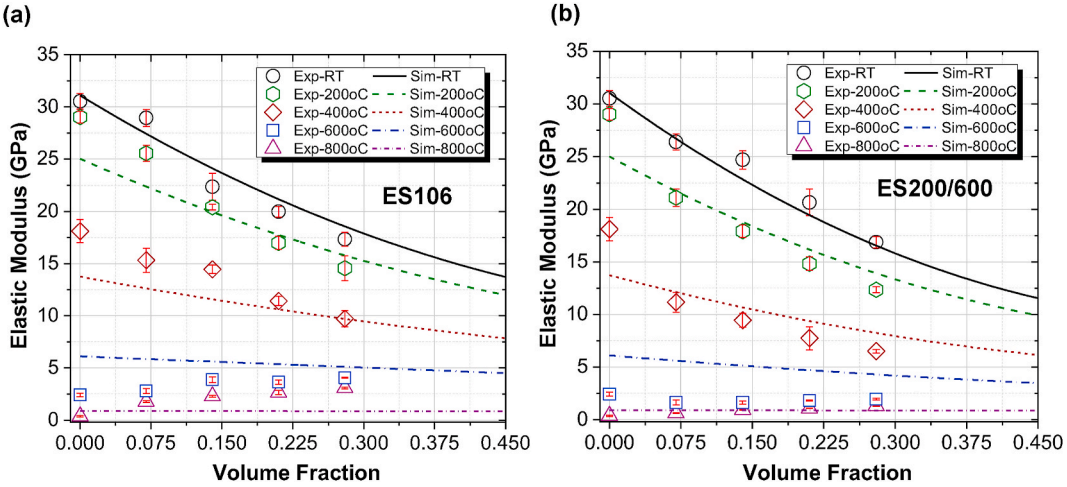

Fig. 13. Effect of particle volume fraction on the elastic modulus of LWCCs: (a) LWCCs containing ES106 FAC; and (b) LWCCs containing ES200/600 FAC.

structures are considered – namely, the cement paste level, and the CSP-filled mortar level. At the cement paste level, the dehydration kinetics including thermal decompositions of C–S–H product and calcium hydroxide are taken into account. In addition, thermal cracking of the matrix is represented by a crack density factor as a function of temperature. At the composite (CSP-filled mortar) level, a sub-stepping homogenization scheme is used to determine the effective properties, where the interfacial damage between cement matrix and inclusion is considered by using a spring–interface model. Based on the combined experimental and simulation study, the following conclusion are drawn:

- The proposed multiscale sub-stepping homogenization model is capable of considering multi-phase thermal deterioration including the thermal decomposition of cement hydration products (i.e., AFt, CH, C–S–H), microcracking of cement paste, and thermal degradation of inclusions, as well as the damage within the interfacial transition zone after exposure to elevated temperature.

- While thermal damage and dehydration starts around 110 °C, significant reduction in compressive strength and elastic modulus were observed for specimens exposed to 400 °C and above. At 600 °C, the compressive strength reductions for LWCCs having 7%, 14%, 21%, and 28% ES106 FAC and ES200/600 FAC are in the range of 48.9%–76.2%. On the other hand, the elastic modulus reductions are in the range of 76.5%–93.8% at 600 °C. Thermal conductivities show continuous trend of decreasing as functions of the exposed temperature.
- The interface damage between inclusion and cement paste matrix plays an important role for the prediction of composite properties, especially at higher temperatures. The ITZ damage parameters are influenced by both the particle type (chemical/surface composition) and its size. Silica sand with larger particle size and higher coefficient of thermal expansion generally lead to a more severe interface damage than its FAC counterparts. This is like due to the pozzolanic activity of FAC surface which leads to higher C–S–H concentration in the ITZ.

Declaration of competing interest

The authors declare that they have no known competing financial interests or personal relationships that could have appeared to influence the work reported in this paper.

Acknowledgements

This research is sponsored by US Department of Energy Building Technology Office (DOE Grant# DE-EE0008677) and US National Science Foundation (NSF Grant# CMMI-1663302, CMMI-1954517). The funding supports from DOE and NSF are greatly appreciated. The author would like to thank Mr. Yi Fang for his assistance to conduct the SEM analysis and Dr. Mansoureh Norouzi Rad from Carl Zeiss Microscopy for performing the X-ray microtomography (XRM) analysis.

References

[1] A. Hanif, Z. Lu, Z. Li, Utilization of fly ash cenosphere as lightweight filler in cement-based composites – a review, Construct. Build. Mater. 144 (2017) 373–384, https://doi.org/10.1016/j.conbuildmat.2017.03.188.
[2] A.L. Brooks, H. Zhou, D. Hanna, Comparative study of the mechanical and thermal properties of lightweight cementitious composites, Construct. Build. Mater. 159 (2018) 316–328, https://doi.org/10.1016/j.conbuildmat.2017.10.102.
[3] H. Zhou, A.L. Brooks, Thermal and mechanical properties of structural lightweight concrete containing lightweight aggregates and fly-ash cenospheres, Construct. Build. Mater. 198 (2019) 512–526, https://doi.org/10.1016/j.conbuildmat.2018.11.074.
[4] M. Maalej, S.T. Quek, S.F.U. Ahmed, J. Zhang, V.W.J. Lin, K.S. Leong, Review of potential structural applications of hybrid fiber Engineered Cementitious Composites, Construct. Build. Mater. 36 (2012) 216–227, https://doi.org/10.1016/j.conbuildmat.2012.04.010.
[5] X. Huang, R. Ranade, Q. Zhang, W. Ni, V.C. Li, Mechanical and thermal properties of green lightweight engineered cementitious composites, Construct. Build. Mater. 48 (2013) 954–960, https://doi.org/10.1016/j.conbuildmat.2013.07.104.
[6] A. Hanif, Z. Lu, Y. Cheng, S. Diao, Z. Li, Effects of different lightweight functional fillers for use in cementitious composites, Int. J. Concr. Struct. Mater. 11 (2017) 99–113, https://doi.org/10.1007/s40069-016-0184-1.
[7] K.J. Krakowiak, R. Gopal, A. Moshiri, T. Phatak, D. Stefaniuk, L. Sadowski, et al., Engineering of high specific strength and low thermal conductivity cementitious composites with hollow glass microspheres for high-temperature high-pressure applications, Cement Concr. Compos. 108 (2020) 103514, https://doi.org/10.1016/j.cemconcomp.2020.103514.
[8] K. Vijay, M. Murmu, S.V. Deo, Bacteria based self healing concrete – a review, Construct. Build. Mater. 152 (2017) 1008–1014, https://doi.org/10.1016/j.conbuildmat.2017.07.040.
[9] J. Gilford, M.M. Hassan, T. Rupnow, M. Barbato, A. Okeil, S. Asadi, Dicyclopentadiene and sodium silicate microencapsulation for self-healing of concrete, J. Mater. Civ. Eng. 26 (2014) 886–896, https://doi.org/10.1061/(ASCE)MT.1943-5533.0000892.
[10] F. Roberz, R.C.G.M. Loonen, P. Hoes, J.L.M. Hensen, Ultra-lightweight concrete : energy and comfort performance evaluation in relation to buildings with low and high thermal mass, Energy Build. 138 (2017) 432–442, https://doi.org/10.1016/j.enbuild.2016.12.049.
[11] M. Robati, G. Kokogiannakis, T.J. Mccarthy, Impact of structural design solutions on the energy and thermal performance of an Australian of fi ce building, Build. Environ. 124 (2017) 258–282, https://doi.org/10.1016/j.buildenv.2017.08.018.
[12] Z. Huang, J.Y.R. Liew, M. Xiong, J. Wang, Structural behaviour of double skin composite system using ultra-lightweight cement composite, Construct. Build. Mater. 86 (2015) 51–63, https://doi.org/10.1016/j.conbuildmat.2015.03.092.
[13] Z. Huang, J.Y.R. Liew, Thin-Walled Structures Structural behaviour of steel – concrete – steel sandwich composite wall subjected to compression and end moment, Thin-Walled Struct. 98 (2016) 592–606, https://doi.org/10.1016/j.tws.2015.10.013.
[14] K.D. Hertz, Concrete strength for fire safety design, Mag. Concr. Res. 57 (2005) 445–453.
[15] Q. Ma, R. Guo, Z. Zhao, Z. Lin, K. He, Mechanical properties of concrete at high temperature — a review, Construct. Build. Mater. 93 (2015) 371–383, https://doi.org/10.1016/j.conbuildmat.2015.05.131.
[16] A. Savva, P. Manita, K.K. Sideris, Influence of elevated temperatures on the mechanical properties of blended cement concretes prepared with limestone and siliceous aggregates, Cement Concr. Compos. 27 (2005) 239–248, https://doi.org/10.1016/j.cemconcomp.2004.02.013.
[17] J. Mindeguia, P. Pimienta, A. Noumowé, M. Kanema, Temperature, pore pressure and mass variation of concrete subjected to high temperature — experimental and numerical discussion on spalling risk, Cement Concr. Res. 40 (2010) 477–487, https://doi.org/10.1016/j.cemconres.2009.10.011.
[18] fib Bulletin No 38, Fire design of concrete structures - materials, structures and modelling. https://doi.org/10.35789/fib.BULL.0038, 2007.
[19] Y.N. Chan, G.F. Peng, M. Anson, Residual strength and pore structure of high-strength concrete and normal strength concrete after exposure to high temperatures, Cement Concr. Compos. 21 (1999) 23–27.
[20] O. Arioz, Effects of elevated temperatures on properties of concrete, Fire Saf. J. 42 (2007) 516–522, https://doi.org/10.1016/j.firesaf.2007.01.003.
[21] J. Xiao, G. Konig, Study on concrete at high temperature in China — an overview, Fire Saf. J. 39 (2004) 89–103, https://doi.org/10.1016/S0379-7112(03)00093-6.
[22] F. Aslani, B. Samali, High strength polypropylene fibre reinforcement concrete at high temperature, Fire Technol. 50 (2014) 1229–1247, https://doi.org/10.1007/s10694-013-0332-y.
[23] B. Chen, J. Liu, Residual strength of hybrid-fiber-reinforced high-strength concrete after exposure to high temperatures, Cement Concr. Res. 34 (2004) 1065–1069, https://doi.org/10.1016/j.cemconres.2003.11.010.
[24] Y. Ding, C. Azevedo, J.B. Aguiar, S. Jalali, Study on residual behaviour and flexural toughness of fibre cocktail reinforced self compacting high performance concrete after exposure to high temperature, Construct. Build. Mater. 26 (2012) 21–31, https://doi.org/10.1016/j.conbuildmat.2011.04.058.
[25] W. Yao, J. Pang, Y. Liu, Performance degradation and microscopic analysis of lightweight Aggregate concrete after exposure to high temperature, Materials 13 (2020) 1–15.
[26] Y.B. Ahn, J.G. Jang, H.K. Lee, Mechanical properties of lightweight concrete made with coal ashes after exposure to elevated temperatures, Cement Concr. Compos. 72 (2016) 27–38, https://doi.org/10.1016/j.cemconcomp.2016.05.028.
[27] A. Al-sibahy, R. Edwards, Thermal behaviour of novel lightweight concrete at ambient and elevated temperatures: experimental , modelling and parametric studies, Construct. Build. Mater. 31 (2012) 174–187, https://doi.org/10.1016/j.conbuildmat.2011.12.096.
[28] Ö. Andiç-çakır, S. Hızal, Influence of elevated temperatures on the mechanical properties and microstructure of self consolidating lightweight aggregate concrete, Construct. Build. Mater. 34 (2012) 575–583, https://doi.org/10.1016/j.conbuildmat.2012.02.088.
[29] A.L. Brooks, Z. Shen, H. Zhou, Development of a high-temperature inorganic synthetic foam with recycled fl y-ash cenospheres for thermal insulation brick manufacturing, J. Clean. Prod. 246 (2020) 118748, https://doi.org/10.1016/j.jclepro.2019.118748.
[30] Z. Huang, J.Y.R. Liew, W. Li, Evaluation of compressive behavior of ultra-lightweight cement composite after elevated temperature exposure, Construct. Build. Mater. 148 (2017) 579–589, https://doi.org/10.1016/j.conbuildmat.2017.04.121.
[31] Z. Huang, K. Padmaja, S. Li, J.Y.R. Liew, Mechanical properties and microstructure of ultra-lightweight cement composites with fly ash cenospheres after exposure to high temperatures, Construct. Build. Mater. 164 (2018) 760–774, https://doi.org/10.1016/j.conbuildmat.2018.01.009.
[32] Y. Zhang, J.W. Ju, H. Zhu, Z. Yan, A novel multi-scale model for predicting the thermal damage of hybrid fiber-reinforced concrete, Int. J. Damage Mech. 29 (2020) 19–44, https://doi.org/10.1177/1056789519831554.
[33] J. Zhao, J. Zheng, G. Peng, K Van Breugel, Prediction of thermal decomposition of hardened cement paste, J. Mater. Civ. Eng. 3 (2012) 592–598, https://doi.org/10.1061/(ASCE)MT.1943-5533.0000423.
[34] J. Zhao, J.J. Zheng, G.F. Peng, A numerical method for predicting Young's modulus of heated cement paste, Construct. Build. Mater. 54 (2014) 197–201, https://doi.org/10.1016/j.conbuildmat.2013.12.070.
[35] C. Jiang, J. Fang, J. Chen, X. Gu, Modeling the instantaneous phase composition of cement pastes under elevated temperatures, Cement Concr. Res. (2020) 130, https://doi.org/10.1016/j.cemconres.2020.105987.
[36] N.I. Voina, D.N. Todor, Thermal analysis of coal and coal ashes, in: C.J. Karr (Ed.), Anal. Methods Coal Coal Prod, vol. II, ACADEMIC PRESS, INC., New York, 1978, pp. 619–648, https://doi.org/10.1016/B978-0-12-399902-3.50024-5.
[37] H. Meradi, L.H. Atoui, L. Bahloul, K. Boubendira, Characterization by thermal analysis of natural kieselguhr and sand for industrial application, Energy Procedia 74 (2015) 1282–1288, https://doi.org/10.1016/j.egypro.2015.07.773.

[38] S. Lim, Effects of Elevated Temperature Exposure on Cement-Based Composite Materials, University of Illinois at Urbana-Champaign, 2015.
[39] C. Alonso, L. Fernandez, Dehydration and rehydration processes of cement paste exposed to high temperature environments, J. Mater. Sci. 9 (2004) 3015–3024.
[40] Z. Shen, H. Zhou, Predicting effective thermal and elastic properties of cementitious composites containing polydispersed hollow and core-shell micro-particles, Cement Concr. Compos. 105 (2020) 103439, https://doi.org/10.1016/j.cemconcomp.2019.103439.
[41] S.E. Gustafsson, Transient diffusivity plane source techniques for thermal conductivity measurements of solid materials and thermal, Rev. Sci. Instrum. 62 (1991) 797–804.
[42] ISO22007-2:2008, Plastics - Determination of Thermal Conductivity and Thermal Diffusivity - Part 2: Transient Plane Source Method, 2008.
[43] Y. He, Rapid thermal conductivity measurement with a hot disk sensor: Part 1. Theoretical considerations, Thermochim. Acta 436 (2005) 122–129, https://doi.org/10.1016/j.tca.2005.06.026.
[44] X.Q. Feng, S.W. Yu, Estimate of effective elastic moduli with microcrack interaction effects, Theor. Appl. Fract. Mech. 34 (2000) 225–233.
[45] H.L. Duan, X. Yi, Z.P. Huang, J. Wang, A unified scheme for prediction of effective moduli of multiphase composites with interface effects. Part I: theoretical framework, Mech. Mater. 39 (2007) 81–93.
[46] L.J. Parrot, D.C. Killoh, Predicting of cement hydration, Br. Ceram. Proc. (1984) 41–53. London, Britain.
[47] B. Lothenback, G Le Saout, E. Gallucci, K. Scrivener, Influence of limestone on the hydration of Portland cement, Cement Concr. Res. 38 (2008) 848–860.
[48] D.P. Bentz, E.J. Garboczi, Percolation of phases in a three-dimensional cement paste microstructural model, Cement Concr. Res. 21 (1991) 325–344.
[49] H.M. Jaeger, S.R. Nagel, Physics of the granular state, Science 255 (1991) 1523–1531, 80-.
[50] R.M. Christensen, K.H. Lo, Solutions for effective shear properties in three phase sphere and cylinder models, J. Mech. Phys. Solid. 27 (1979) 315–330.
[51] Y. Xu, Y.L. Wong, C.S. Poon, M. Anson, Influence of PFA on cracking of concrete and cement paste after exposure to high temperatures, Cement Concr. Res. 33 (2003), https://doi.org/10.1016/S0008-8846(03)00216-3, 2009–16.
[52] N.R. Short, J.A. Purkiss, S.E. Guise, N.R. Short, J.A. Purkiss, Assessment of fire-damaged concrete using crack density measurements, Struct. Concr. 3 (2002) 137–143.
[53] J.D. Eshelby, The continuum theory of lattice defects, Solid. State Phys. - Adv. Res. Appl. 3 (1956) 79–144, https://doi.org/10.1016/S0081-1947(08)60132-0.
[54] B. Klusemann, B. Svendsen, Homogenization methods formulti-phase elastic composites: comparisons and benchmarks, Tech. Mech. 30 (2010) 374–386.
[55] C. Methods, A. Mech, A. Caggiano, G. Etse, Coupled thermo – mechanical interface model for concrete failure analysis under high temperature, Comput. Methods Appl. Mech. Eng. 289 (2015) 498–516, https://doi.org/10.1016/j.cma.2015.02.016.